

# X-ray spectroscopy of the hot gas in the M31 bulge

Jiren Liu<sup>1\*</sup>, Daniel Wang<sup>1</sup>, Zhiyuan Li<sup>2</sup>, John R. Peterson<sup>3</sup>

<sup>1</sup>*Department of Astronomy, University of Massachusetts, Amherst, MA 01002*

<sup>2</sup>*Harvard-Smithsonian Center for Astrophysics, Cambridge, MA 02138*

<sup>3</sup>*Department of Physics, Purdue University, West Lafayette, IN 47907*

## ABSTRACT

We present an X-ray spectroscopic study of the nuclear region of the M31 bulge, based on observations of the *XMM-Newton* Reflection Grating Spectrometers. The obtained high-resolution grating spectra clearly show individual emission lines of highly-ionized iron and oxygen, which unambiguously confirm the presence of diffuse hot gas in the bulge, as indicated from previous X-ray CCD imaging studies. We model the spectra with detailed Monte-Carlo simulations, which provide a robust spectroscopic estimate of the hot gas temperature  $\sim 0.29$  keV and the O/Fe ratio  $\sim 0.3$  solar. The results indicate that iron ejecta of type Ia supernovae are partly-mixed with the hot gas. The observed spectra show an intensity excess at the OVII triplet, which most likely represents emission from charge exchanges at the interface between the hot gas and a known cool gas spiral in the same nuclear region.

**Key words:** ISM: general – Galaxies: individual: M31 – Galaxies: bulge – X-rays: galaxies

## 1 INTRODUCTION

Early-type galaxies and galactic bulges are mainly made up of old stars and evolve passively. Near the end of their life, such stars can collectively eject substantial amounts of matter, which is expected to be heated to the stellar kinematic temperature (typically  $\gtrsim 10^6$  K, e.g., Mathews & Brighenti (2003)). Additional heating by Type Ia SNe can raise the gas temperature further. Ia SNe also provide iron, which can enrich the hot gas substantially. Such a scenario predicts that the metallicity of the hot gas should be similar to the stellar metallicity, which is generally measured to be around solar value (Trager et al. 2000). If the iron ejecta of Ia SNe are well mixed with the hot gas, the resulting iron abundance of the hot gas is then expected to be a factor of a few higher.

However, the expected enrichment of iron from Ia SNe is not detected in observations of elliptical galaxies. For example, Ji et al. (2009) analyzed 10 bright elliptical galaxies with both the data from European Photon Imaging Camera (EPIC) and Reflection Grating Spectrometers (RGS), and they found near-solar abundances in hot gas. For some X-ray-faint galaxies, the fitted abundances generally are below 0.1 solar value (Sarazin, Irwin & Bregman 2001; O’Sullivan & Ponman 2004). It seems both the iron ejecta of Ia SNe and the metals in stellar mass loss are not effectively mixed with, and may be depleted from, hot gas. But it is so far unclear as to whether such apparent metal discrepancies are intrinsic or due to limited quality of the spectral data, or due to over-simplified data analysis and modeling.

M31 is an ideal place for a close examination of hot gas in

a galactic stellar bulge due to the galaxy’s proximity and moderate disk inclination. Prior to *Chandra* and *XMM-Newton*, however, X-ray observations with very limited sensitivities and poor spatial resolutions only allowed a crude study of the X-ray emission in the M31 bulge. For instance, about 15-26% of unresolved emission is attributed to faint sources based on an extrapolation of the luminosity function of detected point sources by *ROSAT* (Primini, Forman & Jones 1993), the remaining unresolved emission is then assumed to arise from the diffuse hot gas. Based on a *XMM-Newton* EPIC MOS1 observation, Shirey et al. (2001) show a significant soft excess in the unresolved emission spectrum compared to the averaged spectrum of resolved sources. This excess may be due to the diffuse hot gas and/or faint sources with soft spectra. Recently, the soft X-ray excess in the M31 bulge has been mapped out with the subtraction of unresolved faint sources by assuming they spatially follow the stellar K-band light distribution (Li & Wang 2007; Bogdán & Gilfanov 2008). The morphology of the remaining diffuse emission is strikingly different from the stellar distribution and shows a bi-polar shape along the minor axis of the bulge. This strongly suggests that the diffuse emission represents a hot gas outflow from the bulge. To firmly establish the diffuse hot gas nature of the soft X-ray emission, however, one needs to detect the expected line emissions.

The RGS on-board *XMM-Newton* have the unique capability to allow for high-resolution X-ray spectroscopy of moderately extended sources because of their large dispersion power. This is the case for the diffuse hot gas in the M31 bulge. To properly interpret the observed spectra, however, a detailed spatial modeling is necessary, because the hot gas is spatially extended and the instrument response depends on the detector position. We use detailed Monte-Carlo simulations to model the observed RGS spectra, which can be decomposed into three components: the hot gas, the point sources,

\* E-mail: jiren@astro.umass.edu

**Table 1.** *XMM-Newton* RGS observations

ID	t (ks)	$t_{eff}$ (ks)	Obs. date
0112570401	46	29	2000-06-25
0109270101	56	21	2001-06-29
0112570101	64	48	2002-01-06

Here  $t$  is the exposure time while  $t_{eff}$  is the useful time after removing intense flare periods.

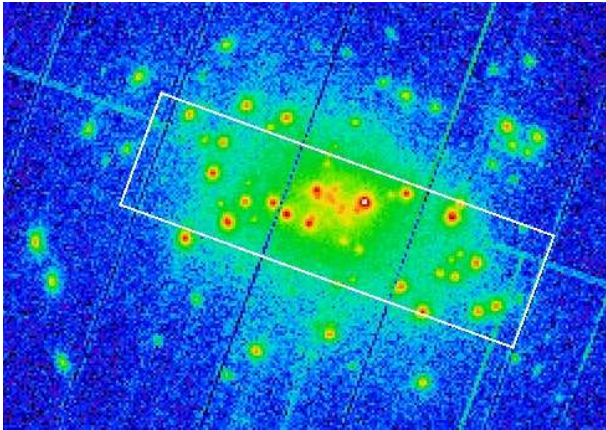


**Figure 1.** RGS dispersion direction over-plotted on a 0.2-12 keV EPIC pn image of the M31 bulge. The long axis direction illustrates the dispersion direction while the short axis is  $4'$ , which is determined by the field coverage of the RGS. The plotted box region is used to extract an EPIC pn spectrum shown in §2.2.

and the background. This then allows us to characterize the thermal and chemical properties of the hot gas, which is the focus of the present paper.

The paper is structured as follows. We describe the observations and our spectral data modeling method in §2. The spectral results are shown in §3. We discuss possible systematic uncertainties in §4 and the implications of our results in §5. The errors quoted are at the 90% confidence level.

## 2 OBSERVATION DATA AND MODELING METHOD

### 2.1 Observation

We use three archival *XMM-Newton* RGS observations listed in Table 1. The total effective exposure time is  $\sim 100$  ks after removing intense flare periods. The most recent version of Science Analysis System (SAS, 9.0) is used for the reduction of photon events.

Two of the three *XMM-Newton* telescopes are equipped with the RGS, each of which is a slit-less dispersive spectrometer. Photons from extended sources are recorded on CCD detectors with the dispersion angle and 1D spatial information along the cross-dispersion direction. The differences of the RGS dispersion directions among the three observations are smaller than  $6.5^\circ$ , and thus, their spectra can be considered approximately from the same source region. The difference in the bore-sights of the three observations along dispersion direction is  $\sim 30''$ , which corresponds to  $0.06 \text{ \AA}$ , far less than the emission line broadening ( $\sim 1 \text{ \AA}$ ) caused by the spatial extent. We merge the events of different observations together and assume the nominal center of the source to be located

between the bore-sights. In Figure 1 we plot the dispersion direction overlaid on a 0.2-12 keV EPIC pn image for one observation (ID 0112570101).

RGS covers an energy range from 5 to  $38 \text{ \AA}$  with the largest effective area around  $15\text{-}20 \text{ \AA}$ . The spectral resolution is  $\sim 0.14\theta \text{ \AA}$ , depending on the angular extent of the observed source,  $\theta$ , in units of arcmin. The 1D spatial resolution is around  $15''$ . As RGS1 and RGS2 are not identical, separate response files are needed for each unit. Thus we will analyze the RGS1 and RGS2 spectra separately. We only consider the first-order photons in extracting the spectra.

Figure 2 presents the RGS1 CCD image merged from all the three observations. It shows clearly the emission lines of highly ionized iron (at 15 and  $17 \text{ \AA}$ ) and oxygen (at 19 and  $22 \text{ \AA}$ ). The broadening of the lines is mainly due to the spatial extent of the X-ray emission of the M31 bulge.

### 2.2 Modeling method

For a point source, the intrinsic spectral model can be convolved with a redistribution matrix function (RMF) and be compared with the observed spectrum using software like XSPEC (Arnaud 1996). For M31, the observed X-ray photons are from an extended region, and the RMF depends on the angular position. The 3D convolution of the angular-dependent RMF is impractical to compute directly, but can be evaluated through a Monte Carlo method. We use the X-ray Monte Carlo code (XMC) developed by Peterson, Jernigan & Kahn (2004) to model the observed RGS spectra of M31. XMC has been used in studies of elliptical galaxies and galaxy clusters (e.g., Peterson et al. 2001; Xu et al. 2002; Peterson et al. 2003; Andersson et al. 2009).

Briefly, XMC generates Monte Carlo photons from a spatial plasma model weighted by its local emissivity, projects them onto the sky, propagates them through an instrument, and predicts their detector positions and energies to be detected by the CCDs. The instrument Monte Carlo models the angular-dependent RMF and the details of its modeling are described in Peterson et al. (2004). The simulated data are selected in the same way as applied to the observed data, and the two data sets can then be compared with each other. The process is repeated by iterating model parameters until an acceptable fit is obtained. In order to reduce the noise of the Monte Carlo sampling, the number of simulated photons is chosen to be 50 times higher than the observed photons (29000 for RGS1 and 30000 for RGS2). The calculation of the gas emissivity calls the XSPEC vpec model (version 1.3.1, Smith et al. 2001). Since the M31 bulge covers all the field of view of the RGS detector, we can not extract a background spectrum. The SAS task rgsbkg-model over-predicts the background component, because part of the emission of the M31 bulge is regarded as the background intensity by rgsbkgmodel. Thus, we use a semi-empirical model, which includes soft protons, detector readout noises, and in-flight calibration sources. The background model is calibrated on blank sky Lockman Hole observations and is used to randomly generate the background events. For the full details of the background modeling we refer to Peterson (2003, section 3.4).

The spectrum of the X-ray emission in the M31 bulge has a prominent power-law component and a soft component (Shirey et al. 2001; Figure 3). The power-law component comes mostly from low-mass X-ray binaries (LMXB) with X-ray luminosities  $\gtrsim 10^{35} \text{ ergs s}^{-1}$ , and a minor fraction ( $< 10\%$ ) is from fainter sources, chiefly cataclysmic variables (CV) and coronally active binaries (AB) (Li & Wang 2007; Bogdán & Gilfanov 2008). Such faint sources also contribute soft photons. But their contribution

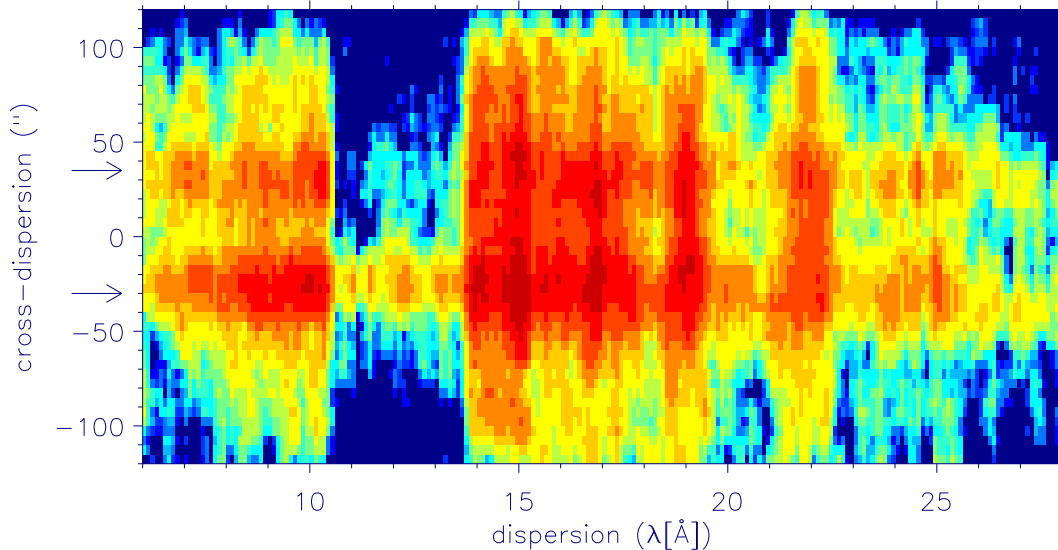


**Figure 2.** Cross-dispersion vs dispersion RGS1 CCD image of the M31 bulge. The trough between 10 and 14 Å is due to the failed CCD7 after Sep. 2000. The positions of two luminous sources are marked with arrows. Emission lines are clearly seen as vertical contours.

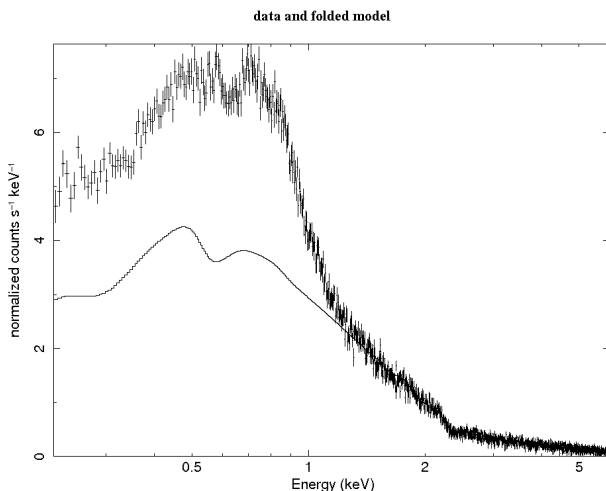


**Figure 3.** EPIC pn spectrum of the M31 bulge overlaid with a power-law model. The spectrum is extracted from the region plotted in Figure 1, and the local background is subtracted. The spectrum above 1.2 keV is well fitted with a power-law model with index 1.67.

to the soft excess at energies  $< 1$  keV (excluding the power-law component) is estimated to be about 5%, based on the low-mass, gas-poor elliptical galaxy of M32. We neglect this contribution in our analysis (more discussion in §4.3). Therefore, we model the observed spectra with three components: the diffuse hot gas, the power-law component, and the background.

We approximate the electron density distribution with a  $\beta$ -model

$$n_e \propto \left[1 + \left(\frac{r}{r_c}\right)^2\right]^{-3\beta/2}, \quad (1)$$

where  $\beta = 0.49$  and  $r_c = 54''$  are from the fitting to the surface density profile of the hot gas (Li & Wang 2007). The normalization of the hot gas is described in the next section.

We characterize the power-law component from an EPIC pn spectrum (Figure 3), which is extracted from the observation of ID

0112570101 over the region plotted in Figure 1. The spectrum includes all the emissions from the point sources and the hot gas. At energies higher than 1.2 keV, the spectrum can be well fitted by a power-law spectrum with index 1.67. This index is assumed for the power law component. As can be seen from Figure 1, bright point sources are scattered around the M31 bulge, and we assume a uniform sphere for the spatial distribution of the power-law component. The effects of the modeling of the power-law component are discussed in §4.2. The maximum radii of both the hot gas and the power-law component are limited to  $8'$ , within which the bulk of the X-ray emission arises. Both components are assumed to be subjected to a foreground absorption of the Galactic column density  $N_H = 6.7 \times 10^{20} \text{ cm}^{-2}$  in the direction of M31.

### 3 RESULTS

Figure 4 presents the RGS1 and RGS2 spectra of the M31 bulge. Note XMC compares the raw counts of the observed and the simulated data in CCD detector directly. We concentrate on the wavelength range between 6–28 Å, which optimizes the signal to noise ratio for our spectral analysis. Individual emission lines from highly ionized iron and oxygen can be clearly seen above the continuum, unambiguously confirming the optically-thin thermal origin for the soft component.

As the spectrum of the soft component is dominated by emission lines (Figure 4), the absolute measurement of the metal abundances of the thermal plasma is hard to obtain due to their sensitive dependence on the continuum estimation. In contrast, the measurement of an abundance ratio, which is determined by the ratio of relevant emission lines, can be more robust. Since the most significant spectral features of the raw RGS spectra are from oxygen and iron, we take  $Z_{\text{Fe}}$  and O/Fe as free parameters. The abundances of other elements are assumed to be the same as iron. (The only other elements showing emission lines are nitrogen (24.8 Å) and neon (12.1 and 13.7 Å), which will be discussed in §4.4.) Thus, we have a total of five free parameters: two normalization parameters  $f_p$  and  $f_b$ , which are the fraction of total photons from the

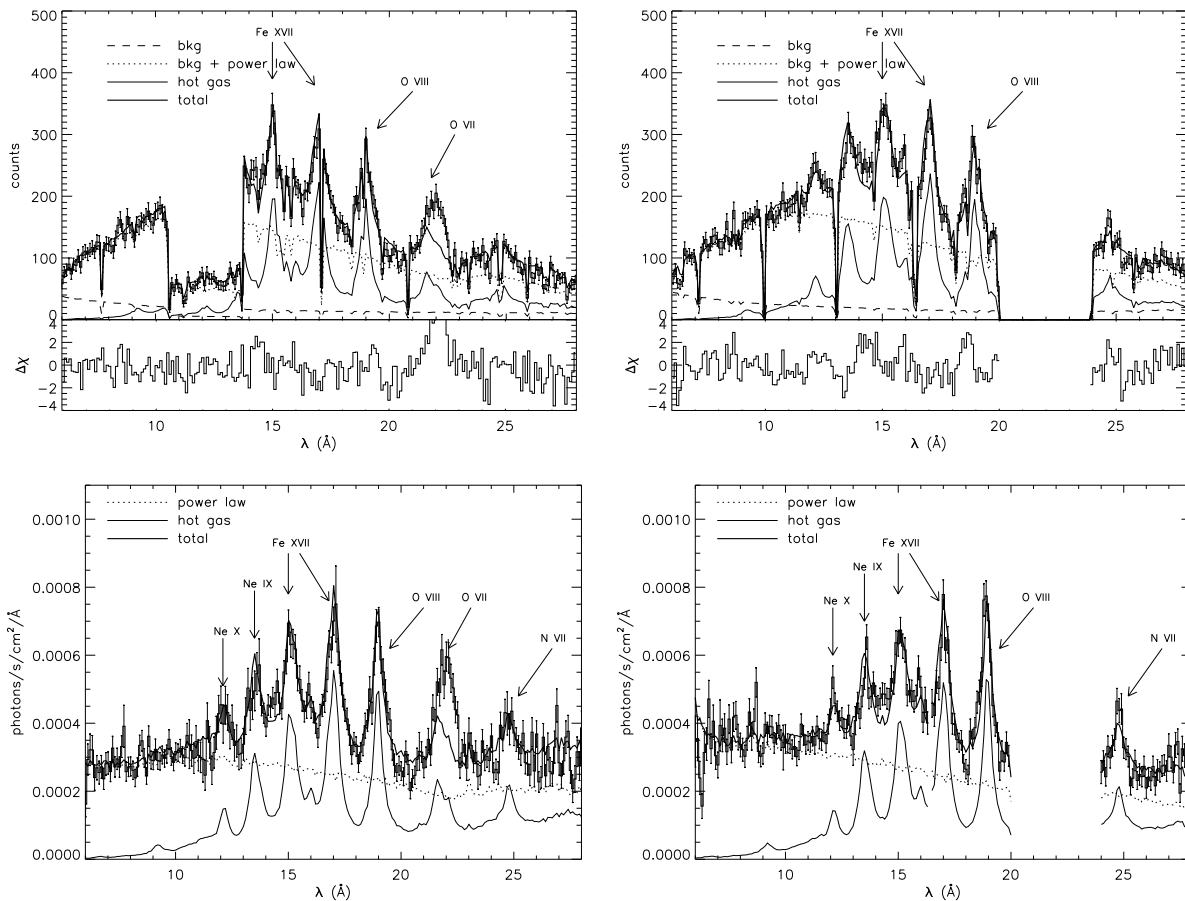


**Figure 4.** RGS1 (left) and RGS2 (right) spectra of the M31 bulge. Top panels are for raw counts, which are used to compare between observed and modeled data; bottom panels present the background-subtracted spectra corrected for the instrument effective area. The histograms are observed spectra. Note the trough region around 10–14 Å of RGS1 is due to the failed CCD7 after Sep. 2000 and the blank region around 20–24 Å of RGS2 is due to the failed CCD4; the sharp absorption features in the raw counts are due to bad columns and gaps between CCDs.

power-law component and the background, respectively (the normalization of the hot gas is then  $1 - f_p - f_b$ ), and three parameters of the hot gas,  $T$ ,  $Z_{\text{Fe}}$ , and  $\text{O}/\text{Fe}$ . The abundances are in units of solar values adopted from Anders & Grevesse (1989). As the photons are from an extended region, the parameters should be considered as averaged quantities.

We note that the spectra below 10 Å are insensitive to the hot gas and are mainly determined by the power-law component and the background (Figure 3, 4). Since the spectral shape of both the power-law component and the background are fixed, it allows us to separate the normalization parameters of  $f_p$  and  $f_b$  from the parameters of the hot gas. We first fit  $f_p$  and  $f_b$  by calculating  $\chi^2$  only in the wavelength range of 6–10 Å with the parameters of the hot gas listed in Table 2. The fit is insensitive to the exact parameter values of the hot gas as long as its contribution to the spectrum in 6–10 Å is small. Then we fix the fitted values of  $f_p$  and  $f_b$ , and fit the parameters of the hot gas,  $T$ ,  $Z_{\text{Fe}}$ , and  $\text{O}/\text{Fe}$ . This separation of the parameter fitting slightly underestimates the parameter errors, but saves computational time substantially, as the Monte Carlo calculation is computationally expensive. The fitting results of both RGS1 and RGS2 data are listed in Table 2 and plotted in Figure 4. The observed RGS1 spectra show excess emissions around the OVII triplet, which need to be treated separately (see below), and

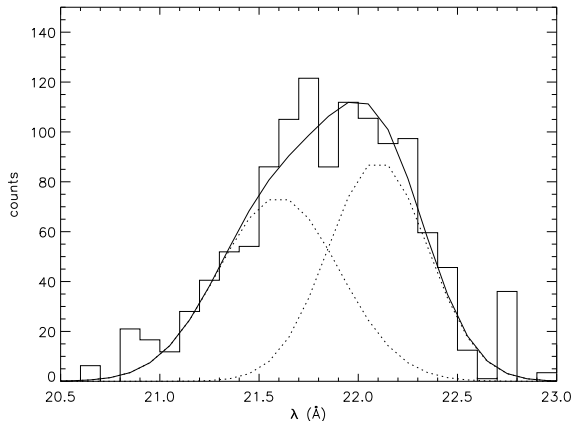
we thus exclude the region of 21.5–22.5 Å in the fit to the RGS1 spectrum.

Figure 4 shows that the RGS1 and RGS2 spectra at energies  $\lesssim 10$  Å are well fitted by adjusting the normalization parameters,  $f_p$  and  $f_b$ , and the emission lines at longer wavelengths also show reasonably good fits to the thermal plasma model. The combination of the three components generally fits well to the observed spectra except for several energy regions with large deviations, which we discuss below. The fitting of the RGS2 spectrum is poorer than RGS1 spectrum. It is mainly due to the large deviations at 13 and 16 Å, where the CCD edges locate.

The most apparent deviation of the observed RGS1 spectrum from the modeled one is the excess around 22 Å, where the helium-like OVII triplet lines occur. This excess, extending through much of the cross-dispersion range (Figure 2), could not be due to any point sources. One plausible explanation is that the excess represents the helium-like OVII triplet lines enhanced by a charge exchange contribution (see §5). Figure 5 presents a decomposition of the observed OVII triplet complex. As the forbidden line is blended with the resonant line, it is difficult to study the detailed line ratios. The data also provide no useful constraint on the normally weak inter-combination line (21.8 Å). We thus fit the observed line profile with two Gaussians centered on 21.6 and 22.1 Å, which correspond to the wavelengths of the resonant and the forbidden

**Table 2.** Fitting results

	$f_p$	$f_b$	$\chi^2/dof$	T (keV)	$Z_{Fe}$	O/Fe	$\chi^2/dof$
RGS1	$0.57 \pm 0.03$	$0.11 \pm 0.02$	45/43	$0.29 \pm 0.02$	$0.13 \pm 0.02$	$0.3 \pm 0.03$	236/214
RGS2	$0.57 \pm 0.03$	$0.12 \pm 0.02$	56/43	$0.28 \pm 0.02$	$0.14 \pm 0.02$	$0.32 \pm 0.03$	293/185



**Figure 5.** RGS spectrum of the OVII triplet complex fitted with two Gaussians. The background and the power-law component have been subtracted; a continuum, which is calculated as the mean in the line wing regions, has also been subtracted. The solid line is the sum of the fitted two Gaussians.

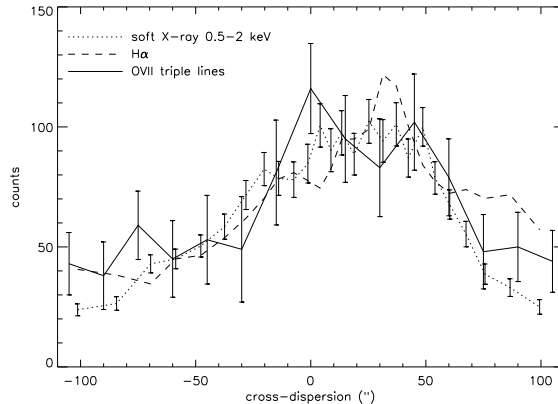
lines, respectively. Both the dispersion and normalization of the two Gaussians are allowed to vary. The fitted intensity ratio of the forbidden line to the resonant line is  $1.46 \pm 0.22$ . The ratio of  $G = (i + f)/r$  (ratio of the sum of the inter-combination and the forbidden lines to the resonant line) for a thermal plasma at temperature of 0.3 keV is  $\sim 0.7$  (e.g., Pradhan 1982) and is  $\sim 2.2$  for the charge exchange emission (Beiersdorfer et al. 2003). Here the ratio we fitted is approximately  $f/(i + r)$ , which is smaller than the ratio  $G$ . Then the actual ratio  $G$  should be larger than 1.46. Thus the intensity ratio suggests a multiple-origin of the observed OVII triplet.

Figure 6 compares the 1D intensity profile of the OVII triple lines along the cross-dispersion direction with those of the soft X-ray emission from hot gas and the H $\alpha$  emission from cool gas. The three profiles are consistent with each other within the statistical errors, indicating that these emission components may be closely related.

Another significant deviation of the observed spectrum from the model is near 14.5 Å. This deviation is possibly due to our simplified modeling of the power-law component or due to the residual calibration errors, which are around 10%. The residual calibration errors are also likely to explain several weaker discrepancies between the RGS2 and the model spectrum like the ones near 13.3 and 16 Å, which occur near CCD edges.

## 4 ROBUSTNESS OF THE RESULTS

We now examine the robustness of our parameter estimates by considering various systematic uncertainties, which dominate over statistical errors in the above analysis. The normalization parameters  $f_p$  and  $f_b$  depend on the spectral shape of the background



**Figure 6.** Intensity profile of the OVII triple lines along the cross-dispersion direction. The line intensity is calculated from the 21–23 Å range after subtracting the continuum estimated from the intensities detected in the line wing regions in the 20–21 Å and 23–24 Å ranges. Also plotted are the 1D intensity profiles of the truly diffuse emission in the *Chandra* ACIS-I 0.5–2 keV band and the H $\alpha$  emission (Li et al. 2009); both are averaged over a 200'' region (where the H $\alpha$  is significant) along the dispersion direction and scaled to the OVII intensity at  $-60''$ .

and the power-law component. Both the temperature and the abundance ratio are mainly determined by the relative strengths of various emission lines and are robust. The absolute iron abundance  $Z_{Fe}$  is determined from the contrast of emission lines to the thermal continuum. Because the emission lines dominate the thermal spectrum, uncertainties related to the estimation of the thermal continuum could affect the iron abundance estimation significantly. In this section, we discuss the systematic uncertainties of our analysis and modeling and how they affect the fitted parameters.

### 4.1 Uncertainties in the background modeling

Because the M31 bulge is an extended source and covers all the field of view (FOV) of the RGS, we can not extract the background spectrum from the same observations. Thus, we have used a background spectrum based on the deep survey observations of the blank sky of the Lockman Hole. It is possible that this modeled background deviates from the real background of the observations used here. Nevertheless, the spectral shape of the background is relatively flat and not supposed to change with time. Any small deviation should also be absorbed, at least partially, into the normalization determination of the power-law component.

### 4.2 Uncertainties in modeling the power-law component

The power-law component dominates the spectrum at energies higher than 1 keV and contributes more than half of the total photons at lower energies. A small uncertainty in its modeling will affect the estimation of the thermal continuum significantly.

Many point sources scatter around the bulge region and some of the sources are likely to be time-variable. It is hard to model them individually for the RGS spectra, and we have used an averaged spectrum to model their contributions. Here we study the effect of its modeling by changing the spatial extent and the absorption column density.

We take a point source spatial model for the power-law component and re-do the fitting process. The fitted results for the RGS1 spectrum are listed in the first row of Table 3. The hot-gas fraction is now 37%, compared to 32% for our standard case. Since the number of the observed photons of emission lines are fixed, a higher gas fraction means a larger thermal continuum and hence a lower abundance: 0.09 solar compared to 0.13 solar.

Table 3 also demonstrates the effect due to potential uncertainties in the absorption column density  $N_H$ . We adopted two values around our adopted Galactic foreground column density from the HI measurement, which is averaged on a degree scale. A smaller absorption means a larger contribution of the power-law component to photons at longer wavelengths and leads to a smaller normalization of the hot gas. The hot-gas fraction is only 26% for  $N_H = 0.04 \times 10^{22} \text{ cm}^{-2}$ , which results in a high iron abundance of 0.3, while for  $N_H = 0.1 \times 10^{22} \text{ cm}^{-2}$ ,  $Z_{\text{Fe}}$  is  $\sim 0.07$ .

Clearly, the assumed spatial extent and absorption column density can significantly change the estimation of the absolute metal abundance. But both the temperature and the abundance ratio of the hot gas are hardly affected. This is because the power-law component mainly affects the continuum estimation, not emission lines.

### 4.3 Unresolved soft stellar contribution

As discussed in Li & Wang (2007) and Bogdán & Gilfanov (2008), part of the soft X-ray emission should arise from unresolved CVs and ABs, the effective temperature of which spans a broad range from  $10^6$  to  $10^8$  K. We estimate their contribution by scaling the spectrum of the dwarf elliptical M32, which has a similar stellar population as the M31 bulge and should contain a negligible amount of hot gas because of the galaxy's low mass. The scaling factor is the K-band flux ratio of the two galaxies. We find that the stellar contribution to the soft excess at energies  $< 1$  keV is only about 5% for the M31 bulge. Thus we do not expect significant errors by neglecting this contribution.

### 4.4 About other elements

In previous study, we have tied the abundances of other elements with iron. As can be seen from Figure 4, the only other two elements showing emission lines are nitrogen at 24.8 Å and neon at 12.1 and 13.7 Å. If we allow the nitrogen abundance as free parameter for the RGS1 spectrum, its abundance is  $0.13 \pm 0.02$ ; if we allow the neon abundance as free parameter for the RGS2 spectrum, its abundance is also  $0.13 \pm 0.02$ . That is, the abundances of both nitrogen and neon are more close to iron than oxygen. This justifies the grouping method we used and indicates that oxygen is less effectively mixed with the hot gas than nitrogen and neon, if they have similar abundances in the stellar ejecta.

## 5 DISCUSSION

We have presented the RGS spectra of the M31 bulge. The observed spectra show prominent emission lines of highly ionized

iron and oxygen and unambiguously confirm the thermal origin of the soft excess inferred from previous imaging and low-resolution spectral analysis. We have further studied the properties of the hot gas. Our measurements of the temperature and the O/Fe ratio of the hot gas are relatively robust, but the fitted absolute abundance has large uncertainties.

The stellar velocity dispersion of the M31 bulge is 156 km/s (Lawrie 1983), which corresponds to a kinematic temperature of 0.14 keV. It is only about half of the fitted temperature of 0.29 keV. This indicates additional heating, presumably from Ia SNe. On the other hand, the main part of the SN energy input is presumably escaped in a bipolar outflow as shown in the previous studies (Li & Wang 2007; Bogdán & Gilfanov 2008).

The effect of the Ia SN feedback is also evident in the abundance pattern. The spectroscopy of the integrated stellar light of the M31 bulge shows a super-solar  $\alpha/\text{Fe}$  ratio (Puzia, Perrett & Bridges 2005). Theoretical modeling also predicts an enhanced abundance of oxygen relative to iron for stars in bulges (Matteucci, Romano & Molaro 1999). Thus our fitted O/Fe ratio of  $\sim 0.3$  for the hot gas in the M31 bulge suggests the iron enrichment by Ia SNe. Otherwise, oxygen has to be significantly depleted from the hot gas.

If the iron ejecta of Ia SNe are completely mixed with the hot gas, the expected iron abundance of the hot gas should then be about 6 times of the solar value (Bogdán & Gilfanov 2008). While our measurement of  $Z_{\text{Fe}}$  is not well constrained, it seems to prefer a sub-solar value. This is similar to various existing observations of hot gas in faint elliptical galaxies (e.g., Sarazin et al. 2001; O'Sullivan & Ponman 2004). This iron-discrepancy has invoked the examination of the assumption of the complete mixing of iron ejecta (Fujita, Fukumoto & Okoshi 1997; Brighenti & Mathews 2005). Hydro-dynamical simulations show that the degree of Ia SN ejecta mixing with materials from stellar mass loss of evolved stars depends on the dynamic state of the outflow in the bulge region. In a supersonic outflow case, for example, the SN ejecta is hardly mixed with the soft X-ray-emitting surrounding gases (Tang et al. 2009). But in a subsonic outflow case, the hot and low-density ejecta become increasingly mixed with the surrounding medium as they flow outward. This partially-mixing scenario helps to explain the unobserved super-solar iron abundance of the hot gas in the M31 bulge and elliptical galaxies.

However, there are potential other complications. There are significant discrepancies in the observational measurements of the stellar metallicity of M31 bulge stars. While the color-magnitude diagram indicates a metallicity distribution that shows a peak at the solar value with a steep decline at higher metallicities and a gradual tail to lower metallicities (Sarajedini & Jablonka 2005), planetary nebulae appear to have a mean oxygen abundance around 0.35 to 0.5 solar value (Jacoby & Ciardullo 1999; Stasińska, Richer & McCall 1998) and rarely show super-solar oxygen abundances. Because planetary nebulae are directly related to the hot gas studied here, we should probably take their average oxygen abundance of 0.4 solar as the representative value. This, together with our measured O/Fe ratio, results in an iron abundance of  $\sim 1$  solar for the hot gas. This value is still below the expected super-solar iron abundance, supporting the partly-mixing scenario.

Finally, we have presented the evidence for a significant charge exchange contribution to the OVII triplet. Charge exchange occurs at interfaces between highly ionized and neutral gases. The presence of neutral gas is apparent in a spiral structure with an overall dimension of  $\sim 4'$ , comparable to the region from which the RGS spectra are extracted. This structure has been mapped out in mid-infrared dust and  $\text{H}\alpha$  emissions and also contains clumps of

**Table 3.** Spectral fitting results with various power-law parameters

	$f_p$	$f_b$	$\chi^2/dof$	T (keV)	$Z_{Fe}$	O/Fe	$\chi^2/dof$
point	0.53±0.03	0.1±0.02	50/43	0.29±0.02	0.09±0.02	0.3±0.03	300/214
$N_H=0.04$	0.63±0.03	0.11±0.02	31/43	0.29±0.02	0.3±0.06	0.31±0.03	241/214
$N_H=0.1$	0.47±0.03	0.12±0.02	30/43	0.29±0.02	0.07±0.02	0.31±0.03	258/214

Note:  $N_H$  is in units of  $10^{22}$  cm $^{-2}$  and point represents the point source spatial model.

molecular gas (Li et al. 2009 and references therein). The 1D intensity profiles of OVII triplet, the H $\alpha$  emission, and the diffuse 0.5-2 keV emission are consistent with each other, indicating that these emission components may be closely related. Similar evidence for charge exchange has also been presented in the RGS spectrum of the starburst galaxy M82 (Ranalli et al. 2008). We are currently systematically investigating such phenomena and its implications for the interplay between the hot and cool gases.

#### ACKNOWLEDGMENTS

We thank the referee for useful comments. This research has made use of *XMM-Newton* archival data. *XMM-Newton* is an ESA science mission with instruments and contributions directly funded by ESA Member States and the USA (NASA). This research is partially supported by NASA/SAO through the grant GO8-9088B.

#### REFERENCES

- Anders, E. & Grevesse, N. 1989, *Geochimica et Cosmochimica Acta*, 53, 197
- Andersson, K., Peterson, J. R., Madejski, G., & Goobar, A. 2009, *ApJ*, 696, 1029
- Arnaud, K. A. 1996, *Astronomical Society of the Pacific Conference Series* v101, *Astronomical Data Analysis Software and Systems V*, ed. Jacoby, G. H. and Barnes, J. 17
- Beiersdorfer, P., Boyce, K. R., Brown, G. V., Chen, H., et al. 2003, *Science*, 300, 1558
- Bogdán, Á. & Gilfanov, M. 2008, *MNRAS*, 388, 56
- Brighenti, F. & Mathews, W. G. 2005, *ApJ*, 630, 864
- Fujita, Y., Fukumoto, J., & Okoshi, K. 1997, *ApJ*, 488, 585
- Jacoby, G. H. & Ciardullo, R. 1999, *ApJ*, 515, 169
- Ji, J., Irwin, J. A., Athey, A., Bregman, J. N., & Lloyd-Davies, E. J. 2009, *ApJ*, 696, 2252
- Lawrie, D. G. 1983, *ApJ*, 273, 562
- Li, Z. & Wang, Q. D. 2007, *ApJ*, 668, L39
- Li, Z., Wang, Q. D., & Wakker, B. P. 2009, *MNRAS*, 397, 148
- Mathews, W. G. & Brighenti, F. 2003, *ARA&A*, 41, 191
- Matteucci, F., Romano, D., & Molaro, P. 1999, *A&A*, 341, 458
- O'Sullivan, E. & Ponman, T. J. 2004, *MNRAS*, 349, 535
- Peterson, J. R., Kahn, S. M., Paerels, F. B. S., Kaastra, J. S., Tamura, T., Bleeker, J. A. M., Ferrigno, C., & Jernigan, J. G. 2003, *ApJ*, 590, 207
- Peterson, J. R. 2003, Ph.D thesis, Columbia Univ
- Peterson, J. R., Paerels, F. B. S., Kaastra, J. S., Arnaud, M., et al. 2001, *A&A*, 365, L104
- Peterson, J. R., Jernigan, J. G., & Kahn, S. M. 2004, *ApJ*, 615, 545
- Pradhan, A. K. 1982, *ApJ*, 263, 477
- Primini, F. A., Forman, W., & Jones, C. 1993, *ApJ*, 410, 615
- Puzia, T. H., Perrett, K. M., & Bridges, T. J. 2005, *A&A*, 434, 909
- Ranalli, P., Comastri, A., Origlia, L., & Maiolino, R. 2008, *MNRAS*, 386, 1464
- Sarajedini, A. & Jablonka, P. 2005, *AJ*, 130, 1627
- Sarazin, C. L., Irwin, J. A., & Bregman, J. N. 2001, *ApJ*, 556, 533
- Shirey, R., Soria, R., Borozdin, K., Osborne, J. P., et al. 2001, *A&A*, 365, L195
- Smith, R. K., Brickhouse, N. S., Liedahl, D. A., & Raymond, J. C. 2001, *ApJ*, 556, L91
- Stasińska, G., Richer, M. G., & McCall, M. L. 1998, *A&A*, 336, 667
- Tang, S., Wang, Q. D., Mac Low, M., & Joung, M. R. 2009, *MNRAS*, 398, 1468
- Trager, S. C., Faber, S. M., Worthey, G., & González, J. J. 2000, *AJ*, 120, 165
- Xu, H., Kahn, S. M., Peterson, J. R., Behar, E., et al. 2002, *ApJ*, 579, 600